Sound Generation by Turbulence in Simulated Rocket Motor Cavities

U. G. Hegde* and W. C. Strahle†

Georgia Institute of Technology, Atlanta, Georgia

The present investigation is motivated by vibration problems in solid-propellant rocket motors. A class of interior flows modeled to simulate flow conditions inside rocket motor cavities is considered. The turbulence generated pressure fluctuation consists of two components, acoustic and hydrodynamic. The Bernoulli enthalpy theory of aeroacoustics is employed to extract acoustic pressure spectra from experimentally obtained turbulence data and acoustic impedance values at flow boundaries. The effects of turbulence intensities, sidewall acoustic impedance, length-to-diameter ratio of the cavity, and different mass flux on the acoustic pressure level are investigated in experimental configurations. Typical pressure levels inside rocket motor environments are calculated utilizing the A-B representation for propellant response.

Nomenclature

a = tube radius
A = tube cross-section area, parameter in Eq. (18)
B = parameter in Eq. (18)
c = isentropic speed of sound
f = quantity defined by Eq. (5)
$F(\omega)$ = frequency correction factor
g_0 = Green's function for the Bernoulli enthalpy problem
g_ω = Green's function for the acoustics problem
g_T = inverse Fourier transform of $k^2 g_\omega$
h = specific enthalpy
H = Bernoulli enthalpy
H_0 = cross-section average of Bernoulli enthalpy fluctuations
k = wave number
k_{00} = modified wave number
ℓ = duct length
l_{corA} = correlation length in axial direction
M_e = mean Mach number at nozzle entrance plane
M_0 = mean Mach number at head end
M_r = mean radial Mach number at propellant surface
n = index in burning rate law
p = pressure
p_H = hydrodynamic pressure fluctuation
p_Φ = acoustic pressure fluctuation
$Q(x)$ = factor in Eq. (16)
r = radial coordinate, propellant burning rate
r = two-dimensional polar coordinate
R = defined by Eq. (20)
R_T = inverse Fourier transform of R
s = specific entropy
S_{00} = defined by Eq. (13)
$S_{\Phi\Phi}$ = acoustic pressure auto spectrum
S_{ij} = cross-power spectrum between signals i and j
t = time
T_ω = defined by Eq. (12)
u = incompressible field velocity vector
$\bar{U}_l$ = mean axial velocity
$\bar{U}_{lc}$ = cross section averaged axial velocity
v = total velocity vector

v_a = acoustic velocity vector
V = tube volume
x,x_0 = axial coordinate
z = axial separation coordinate
α_s = thermal diffusivity of propellant
β = sidewall/propellant specific acoustic admittance
β_{crit} = critical β for stability analysis
γ = ratio of specific heats
δ = Dirac delta function
χ = wall loss factor
Φ = acoustic potential, azimuthal coordinate in Eq. (15)
Λ = defined by Eq. (18)
ρ = density, radial coordinate in Eq. (15)
ρ_0 = reference state density
$\bar{\rho}_g$ = mean density of gaseous products from combustion
$\bar{\rho}_s$ = mean density of solid propellant
λ = acoustic wavelength
λ_{00} = modified acoustic wavelength
ζ_e = specific acoustic impedance at nozzle entrance plane
ζ_0 = specific acoustic impedance at head end
ω = angular frequency

Superscripts

$(\bar{\ })$ = mean or ensemble or cross-section average
$(\ )'$ = fluctuation
$(\ )^*$ = complex conjugate

Subscripts

i = quantity in ith direction
ω = discrete Fourier transform
l = quantity in axial direction

Introduction

THE issue of pressure fluctuations in interior flows has attracted the attention of the propulsion community due to its relevance to vibration and instability problems in solid-propellant rocket motors.[1] Under normal operating conditions, these fluctuations can be of the order of 1-2% of the mean chamber pressure and are usually random in space and time. However, fluctuations near the acoustic resonant frequencies of the chamber may develop a nearly stationary phase relationship and aggravate the vibration problem.

One source of pressure fluctuations inside rocket motors is the turbulence present within the chamber. Pressure fluctuations associated with the turbulent eddies arise to balance the local, unsteady acceleration. A small part of the turbulence energy can, however, escape in the form of acoustic radiation (Fig. 1). Modification of the acoustic radiation

*Graduate Research Assistant. Student Member AIAA.

†Regents' Professor, Aerospace Engineering. Associate Fellow AIAA.

occurs due to reflections from the nozzle and at the propellant surface and, as a result, a standing wave may be set up in the chamber. The prediction of the pressure levels associated with this standing wave, given sufficient data about the turbulence field and the acoustic properties at the flow boundaries, is the objective of this paper.

The Bernoulli enthalpy approach of Yates and Sandri[2] was applied by Strahle and Neale[3] to the problem of turbulence-generated pressure fluctuations in fully developed turbulent pipe flow. This approach requires splitting the velocity field into its irrotational (potential) and rotational components. An assumption is made in Ref. 3 that the potential component of the velocity is negligible compared to the rotational component. For the pipe flow case, the time-averaged potential velocity may be identified with the cross-section averaged axial velocity and is not negligible compared to the mean rotational component making the above assumption questionable. Yates[4] has modified the Bernoulli enthalpy approach to very low Mach number flows by treating the time-averaged flow as incompressible. The fluctuations about the mean velocity are then split into irrotational and rotational components. A kinematic definition of sound is given by identifying the irrotational component of the velocity fluctuation with the acoustic velocity. The rotational component of the velocity fluctuation is incompressible by definition and along with the mean flow constitutes the incompressible velocity field. This approach is followed here.

Analysis

The configurations of Fig. 2 are considered, which are also the configurations in the experimental results to follow. The majority of the pipe (Fig. 2a) is filled with fully developed turbulent flow (the Reynolds number based on the diameter is 1.1×10^5) and is terminated by a choked nozzle. The porous tube (Fig. 2b) simulates a rocket cavity with the entire mass injected from the sidewalls. In both cases the Mach number at the nozzle entrance plane is about 0.1.

The analysis is developed for very low Mach number flows so that the time-averaged flow is considered incompressible. Fluctuations about the mean velocity are split into rotational and irrotational components. The irrotational component of the velocity fluctation is defined to be the acoustic velocity and the rotational component constitutes part of the incompressible field and is identified with turbulent velocity fluctuations,

$$v = u + v_a, \quad \cdot \nabla \cdot u = 0, \quad v_a = \nabla \Phi \tag{1}$$

The governing equations are[4]

$$\frac{1}{c^2} \frac{D^2 \Phi}{Dt^2} - \nabla^2 \Phi = \frac{1}{c^2} \frac{DH}{Dt} \tag{2}$$

$$\nabla H = -\frac{Du}{Dt} \tag{3}$$

where the Bernoulli enthalpy H is given by

$$H = h + \frac{D\Phi}{Dt} + \frac{|\nabla \Phi|^2}{2}$$

and the operator

$$\frac{D}{Dt} = \frac{\partial}{\partial t} + u \cdot \nabla$$

is the substantial derivative following the nonacoustic motion of the fluid.

Entropy variations have been neglected because it is the larger energy-containing eddies that are responsible for sound generation and these are inviscid to a good approximation.

Magnitude estimates show that acoustic velocities are an order of magnitude below the turbulent velocity fluctuations and are neglected in comparison. Moreover, Eq. (2) has been linearized with respect to the acoustic potential Φ.

Fluctuations about the time-averaged pressure are obtained from the isentropic equation of state

$$dh = dp/\rho$$

In linearized form, this becomes in terms of H and Φ

$$p' = \rho_0 \left(H' - \frac{\partial \Phi}{\partial t} \right)$$

Therefore, the pressure fluctuation consists of two parts, one being associated with Φ and the acoustic velocity. Thus, the acoustic pressure is

$$p_\Phi = -\rho_0 \frac{\partial \Phi}{\partial t} \tag{4}$$

The other part of the pressure fluctuation is associated with H and the incompressible motion and is hence a hydrodynamic fluctuation

$$p_H = \rho_0 H'$$

It is the acoustic pressure p_Φ that will be of interest in the following development.

The nonhomogeneous linear wave equation (2) is to be solved. This requires a knowledge of the H field. The solution for H is obtained by taking the divergence of Eq. (3) and solving the resultant Poisson's equation

$$\nabla^2 H = -\frac{\partial^2 u_i u_j}{\partial x_i \partial x_j} = -f(x_i, t) \tag{5}$$

The boundary condition $\nabla H \cdot n$ is specified from Eq. (3) at the inlet plane, sidewalls, and nozzle entrance plane.
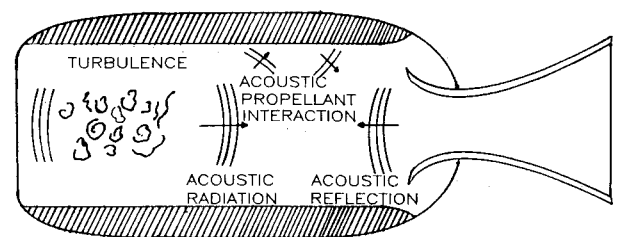

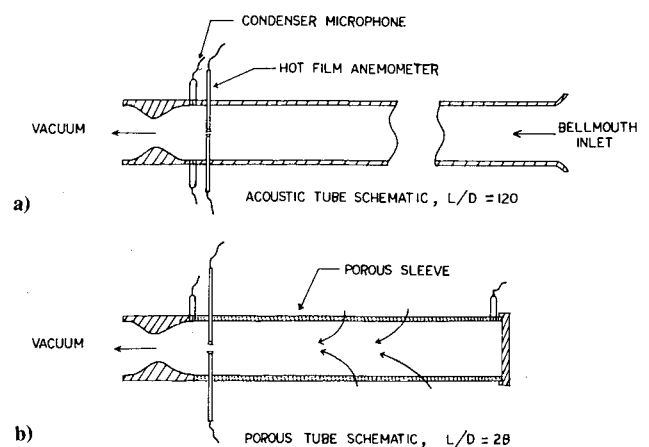Fig. 1 Turbulence-generated pressure fluctuations.

Fig. 2 Schematic diagram of the experimental configurations.

Transverse acoustic modes cut on at frequencies[5] of the order of $c/2a$, whereas the turbulence energy spectrum is significant only to frequencies[6] of the order of $\bar{U}_l/2a$. Thus, for low Mach number flows, the turbulence energy is negligible at transverse acoustic mode frequencies. Therefore, only the cross-section average of Eq. (2) representing plane wave acoustic motion is investigated. Consequently, H is replaced by its cross-section-averaged fluctuation H_0 on the right-hand side of Eq. (2). One way of obtaining H_0 is to construct the Green's function g_0 for the one-dimensional analog of Eq. (5),

$$\frac{d^2 g_0}{dx^2} = -\frac{1}{A}\,\delta(x-x_0)$$

where

$$\delta(x-x_0) = 1 \qquad x=x_0$$

$$= 0 \qquad \text{otherwise}$$

with $g_0=0$ at the inlet (head end) and $dg_0/dx=0$ at the nozzle entrance plane. The solution is

$$g_0(x,x_0) = x_0/A, \quad x \ge x_0$$

$$= x/A, \quad x \le x_0$$

Then H_0 is given in terms of g_0 by

$$H_0(x) = \int_{V_0} g_0 f'(x_{0i},t)\,dV_0 + \int_{A_{\text{surface}}} g_0(\nabla H \cdot n)'\,dA_0 \qquad (6)$$

Simplification of Eq. (6) is facilitated by noting that $\nabla \cdot u = 0$ and that the turbulent velocity fluctuations vanish at the entrance plane and on the sidewalls in all the configurations. For the pipe flow, the inlet flow is a potential flow and all velocities vanish on the walls. For the porous tube flow, there is no flow in at the head end and the low Reynolds number of the flow through the pores of the tube (the pore velocity and pore diameter are of the order of 1 m/s and 10^{-6} m, respectively) indicates that turbulent velocity fluctuations are absent at the tube walls. The solution for H_0 may then be expressed as

$$H_0(x) = -\frac{1}{A}\int (u_l^2)'\,dA \qquad (7)$$

where the integral is over the local cross-section area.

Velocity fluctuations in the experimental configurations are an order of magnitude below the mean velocity. This enables the linearization of Eq. (7)

$$H_0(x) = -\frac{2}{A}\int \bar{U}_l u_l'\,dA$$

Now $\bar{U}_l = \bar{U}_{lc} + (\bar{U}_l - \bar{U}_{lc})$, where $\bar{U}_{lc}$ is constant over the cross section and is defined by

$$\int \bar{U}_l\,dA = \bar{U}_{lc}A$$

Substituting into Eq. (7), the term

$$\int \bar{U}_{lc} u_l'\,dA = \bar{U}_{lc}\int \nabla \cdot u'\,dV = 0$$

because $\nabla \cdot u' = 0$. Hence,

$$H_0(x) = -\frac{2}{A}\int (\bar{U}_l - \bar{U}_{lc}) u_l'\,dA \qquad (8)$$

The acoustic field is obtained from a plane wave equation derived from Eq. (2). As mentioned previously, H is replaced by H_0 on the right side of Eq. (2). A further simplification occurs by noting that the axial length scale of H_0 is that of g_0 and is ℓ (the length of the duct), while its time scale is $a/\bar{U}_l$, where a (the duct radius) is a typical vortical length scale.[6] Accordingly, the partial time derivative of H_0 dominates the convective acceleration terms in DH_0/Dt for large ℓ/a, as in the cases under consideration. Therefore, DH_0/Dt is approximated by simply $\partial H_0/\partial t$. Then, for low Mach numbers, taking the Fourier transform of the cross-section-averaged version of Eq. (2)

$$\frac{d^2\Phi_\omega}{dx^2} + k_{00}^2\bar{\Phi}_\omega = \frac{i\omega}{c^2}H_{0\omega} \qquad (9)$$

where the modified wave number k_{00} is given by

$$k_{00}^2 = k^2 - i(2k\beta/a)$$

and may be approximated by[5]

$$k_{00} = k - i\pi\chi$$

with $k=\omega/c$. Increase in the wall loss factor x signifies increased attenuation of acoustic energy at the sidewalls of the tube.

The boundary conditions on $\bar{\Phi}_\omega$ are[7]

$$\frac{d\bar{\Phi}_\omega}{dx} + \frac{ik}{\zeta_0 + \bar{M}_0}\bar{\Phi}_\omega = 0 \quad \text{at } x=0$$

$$\frac{d\bar{\Phi}_\omega}{dx} + \frac{ik}{\zeta_e + \bar{M}_e}\bar{\Phi}_\omega = 0 \quad \text{at } x=\ell$$

The solution is obtained by using the Green's function g_ω, satisfying

$$\frac{d^2 g_\omega}{dx^2} + k_{00}^2 g_\omega = -\delta(x-x_0)$$

which has the same boundary conditions as $\bar{\Phi}_\omega$. The function g_ω is obtained by standard methods. For example, for the porous tube case with $\bar{M}_0=0$, g_ω at the head end, $(x=0)$ is given by,

$$g_\omega(0,x_0) = -\left[k_{00}\cos k_{00}(\ell-x_0) + \frac{ik}{\zeta_e + \bar{M}_e}\sin k_{00}(\ell-x_0)\right]$$

$$\div \left\{k_{00}\left[\left(k_{00} - \frac{k^2}{\zeta_0 k_{00}(\zeta_e + \bar{M}_e)}\right)\sin k_{00}\ell\right.\right.$$

$$\left.\left. - ik\left(\frac{\zeta_0 - \zeta_e - \bar{M}_e}{(\zeta_e + \bar{M}_e)\zeta_0}\right)\cos k_{00}\ell\right]\right\} \qquad (10)$$

The acoustic potential $\bar{\Phi}_\omega$ is then given by

$$\bar{\Phi}_\omega(x) = -\frac{2i\omega}{Ac^2}\int_{V_0}(\bar{U}_l - \bar{U}_{lc})u_{l\omega}g_\omega(x,x_0)\,dV_0$$

and the acoustic pressure transform, from Eq. (4), by

$$p_{\Phi\omega}(x) = -\frac{2\rho_0 k^2}{A}\int_{V_0}(\bar{U}_l - \bar{U}_{lc})u_{l\omega}g_\omega(x,x_0)\,dV_0 \qquad (11)$$

The autospectrum $S_{\Phi\Phi}$ of the acoustic pressure is obtained by multiplying $p_{\Phi\omega}$ by its complex conjugate and taking an

ensemble average

$$S_{\Phi\Phi}(x) = \frac{\rho_0^2 k^4}{A^2} \int_{V_1} \int_{V_2} g_\omega^*(x,x_1) g_\omega(x,x_2)$$

$$\times \overline{T_\omega^*(x_1) T_\omega(x_2)} dV_1 dV_2$$

where

$$T_\omega(x) = 2(\bar{U}_1 - \bar{U}_{1c}) u_{1\omega}(x) \qquad (12)$$

To estimate $S_{\Phi\Phi}$, the axial correlation length is introduced

$$l_{\text{corA}} = \frac{1}{S_{11}} \int_{-\infty}^{+\infty} S_{12} dz$$

where S_{11} is the autospectrum of T_ω and S_{12} is given by

$$S_{12} = \text{Real} \overline{T_\omega^*(x_0,r) T_\omega(x_0+z,r)}$$

and is the real part of the cross spectrum of T_ω with respect to the axial separation z. The axial correlation lengths have to be obtained experimentally (see Fig. 5 below).

The Green's function g_ω has a length scale of λ, the acoustic wavelength. For frequencies under consideration, $\lambda \gg l_{\text{corA}}$ so that g_ω varies slowly over the distance scale where the axial correlation of T_ω falls to zero. Introducing

$$S_{00}(x) = \left(\frac{\rho_0}{A}\right)^2 \int dA(r_1) \int dA(r_2) \overline{T_\omega^*(x,r_1) T_\omega(x,r_2)} \qquad (13)$$

the expression for $S_{\Phi\Phi}$ is approximated by

$$S_{\Phi\Phi}(x) \simeq k^4 \left[\int_0^\ell S_{00}(x_0) |g_\omega(x,x_0)|^2 dx_0\right] l_{\text{corA}} \qquad (14)$$

To estimate $S_{00}(x)$ the scheme of Ref. 3 is followed, whereby $S_{00}(x)$ is approximated by

$$S_{00}(x) \approx \frac{2\rho_0^2 \pi}{A} \left[\int_0^{a/2} (S_{12})_{\Phi=\pi/2} \rho d\rho + \int_0^{3a/2} (S_{12})_{\Phi=3\pi/2} \rho d\rho\right] \qquad (15)$$

where

$$S_{12} = \text{Real} \overline{T_\omega^*(x,a/2,0) T_\omega(x,\rho,0)}$$

and the coordinate system is described in Fig. 5 of Ref. 3. Obtaining S_{12} experimentally requires fixing an anemometer at half the radius and carrying out a traverse of another anemometer along the diameter defined by the reference probe and the tube center.
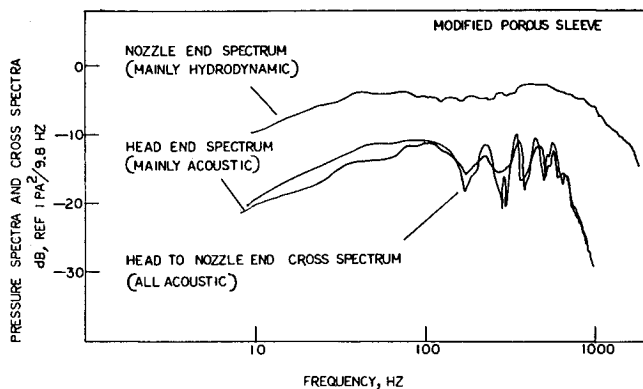
Fig. 3 Wall pressure spectra and cross spectra in modified porous tube.

Experimentally $S_{00}(x)$ was determined for $x = \ell$. For the purposes of estimating $S_{\Phi\Phi}$, it is assumed that

$$S_{00}(x) = S_{00}(\ell) Q(x) F(\omega) \qquad (16)$$

so that $S_{00}(x)$ may be related to $S_{00}(\ell)$. For fully developed turbulent pipe flow, $S_{00}(x)$ will be independent of x so that both $Q(x)$ and $F(\omega)$ are taken to be unity. For the porous tube case, $Q(x)$ is taken to be a second-degree polynomial
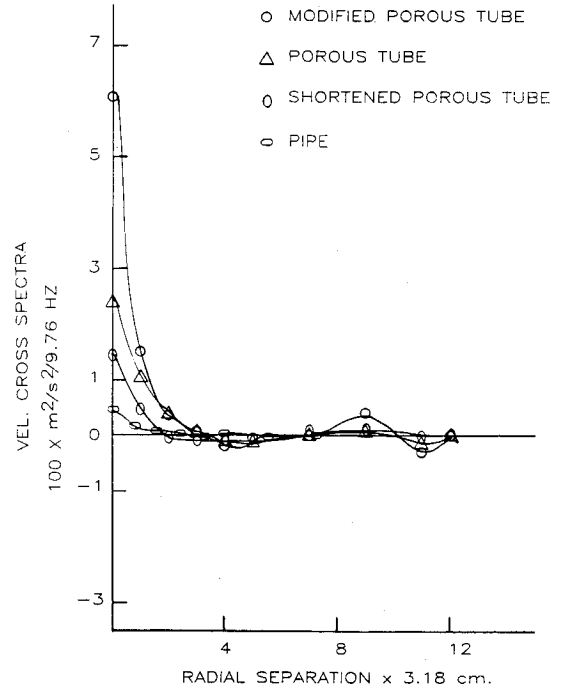
Fig. 4 Cross spectra of axial velocity fluctuations at 100 Hz with respect to radial separation.
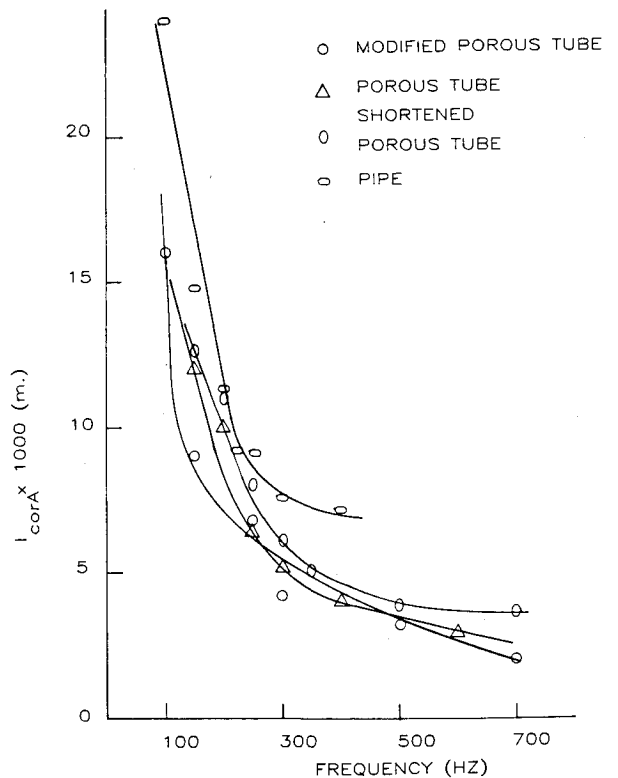
Fig. 5 Axial correlation lengths as a function of frequency.

and is constructed by noting that $S_{00}(0) = 0$, $dS_{00}/dx]_{x=0} = 0$, and $Q(\ell) = 1$. The frequency content is corrected by the factor $F(\omega)$, which is obtained here by considering the autospectrum S_{11} of the fluctuating axial velocity at several axial stations at half-radius,

$$F(\omega) = \frac{1}{n} \sum_{i=1}^{n} S_{11}(x_i) \Big/ S_{11}(\ell), \quad x_N = \ell$$

Typically, $n = 2$ or 3 has been used with the autospectra being measured near the head end and at the half the length of the tube.

Experimental

The pipe in Fig. 2a is 6 m long and 5 cm in diameter. The tube in Fig. 2b is constructed of porous sleeves made of sintered steel and is also 5 cm in diameter. In both cases, the flow exits through a choked nozzle. The pressure drop across the walls of the porous tube is, on the average, about 4500 Pa and is much lower than the pressure drop across the nozzles under choked conditions, insuring that the net mass flux through the nozzle is determined purely by its area ratio. Two other versions of the porous tube were also considered. One was a modified version that had acoustically stiffer walls created by taping alternate 2.5 cm sections along the tube length. The other was a shortened version having a length-to-diameter ratio of 15. In all cases the Mach number at the nozzle entrance plane was about 0.1.

The setups were instrumented with flush-mounted 0.5 in. condenser microphones and hot-film anemometer probes. The hot films could be traversed radially with respect to each other at the same axial location. By means of a 4 mm horizontal slot machined in the sidewalls, one hot-film probe could be moved axially with respect to the other. The wall microphones were used to measure wall pressure spectra and cross spectra. The hot films were used to obtain necessary axial velocity correlations. Signals from the instruments were recorded on magnetic tape and then analyzed in the frequency domain on a Fourier analyzer.

Wall pressure spectra and cross spectra associated with the modified porous tube are shown in Fig. 3. At the head end, where there is no turbulence, the spectrum shows peaks at the resonant acoustic frequencies of the tube. In the spectrum at the nozzle end, the acoustic peaks are lost in the broadband background level. The cross spectrum from the head end to the nozzle end reveals only the acoustic part. A comparison of the head-end spectrum with the head-to-nozzle-end cross spectrum shows both to be of the same level. This strengthens the belief that the head-end spectrum is mainly acoustic, whereas the nozzle-end spectrum is dominated by

hydrodynamic flow noise that is local in nature.[8] Investigations of the noise of fully developed turbulent pipe flows are reported in Ref. 8.

The real part of the axial velocity cross spectra at the nozzle entrance plane at a frequency of 100 Hz referred to a point at the half-radius is plotted in Fig. 4 for the pipe and porous tube configurations. The value for zero separation corresponds to the autospectrum at 100 Hz. Clearly, turbulence levels in the porous tube configurations are higher as compared to those in the pipe.

Typical experimental values of l_{corA} at the nozzle entrance plane at the half-radius are plotted in Fig. 5. This length signifies the axial distance over which turbulence velocity fluctuations are correlated and is of the order of the tube radius. The axial correlation length decreases with frequency, indicating that lower frequency components of the velocity fluctuation are correlated over greater distances.

Acoustic impedance measurements were carried out using the classical impedance tube technique.[5] Figure 6 plots the wall loss factor $(\pi\chi)$ for the porous tube configurations. The wall loss factor for the modified porous tube is the lowest since those sections of the tube that were taped tended to acoustically stiffen the sidewalls. A least squares fit through the data points was deemed to be adequate.

The specific acoustic impedance ζ_e at the nozzle entrance plane was theoretically obtained using the short nozzle approximation. The expression for ζ_e for low Mach numbers is

$$\zeta_e = 2/\bar{M}_e(\gamma - 1) \qquad (17)$$

Comparisons of the predicted acoustic spectra with the wall measured pressure spectra are shown in Figs. 7 and 8. For the pipe flow the comparison is at the nozzle end where the wall measured spectrum contains both hydrodynamic and acoustic components. However, the resonant peaks are clear and definite and a valid comparison can be made. For the porous tube case, the comparison is at the head end where the wall measured spectrum is mainly acoustic.

It is seen in both cases that the resonant frequencies are well predicted and the magnitude of the spectra is predicted to within a factor of three. Since only limited turbulence data were used in the prediction, this factor is acceptable. The most serious discrepancy is with regard to the relative magnitude of the first mode as compared to the other modes for the porous tube case. The experimental spectra show the level at the first mode to be much higher than the levels at the other modes. The predicted spectra for the porous tube does not show this behavior to the degree present in the experimental spectra. Two reasons for this discrepancy may be advanced. First, by using the impedance tube technique, wall loss factors can be measured only near to and above the second natural frequency. Values at lower frequencies were obtained by linear extrapolation and may have been in error to some extent. Second, the frequency correction factor $F(\omega)$ may not be sufficient. In particular, a better estimate of $S_{00}(\ell)$ may be obtained by measuring the cross spectra of the velocity
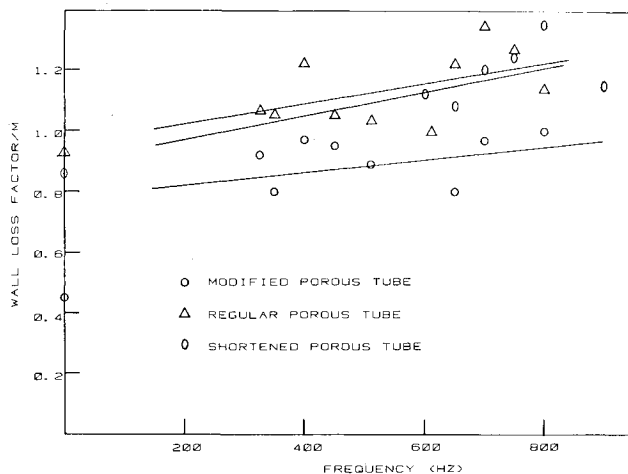

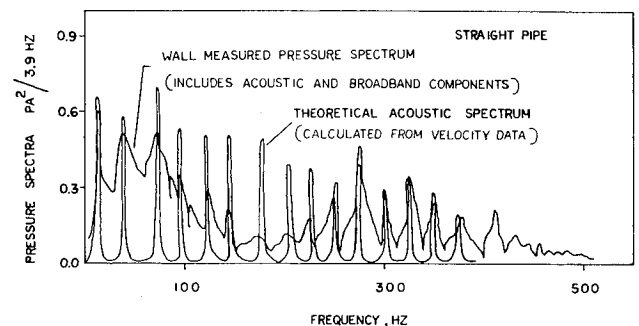Fig. 6   Measured wall loss factors for porous tube configurations.

Fig. 7   Pressure spectra at nozzle entrance plane for pipe flow.

fluctuations with respect to the radial separation for more than one representative point. In other words, the limited amount of turbulence data used could also be responsible for the discrepancy.

Application to Rocket Motors

The present theory may be extended to center-perforated solid rocket motors by identifying β, the sidewall specific acoustic admittance with the propellant admittance. The propellant admittance has been modeled here by the A-B representation of the propellant response.[9] For simplicity, it is assumed that fluctuations at the burning surface of the propellant are isentropic. Then, in terms of the A-B model

$$\beta = -\bar{M}_r \left[\frac{\gamma n A B}{\Lambda + (A/\Lambda) - (1+A) + AB} - 1 \right] \quad (18)$$

where

$$\Lambda = \frac{1}{2} + \left[\frac{1}{4} + \frac{i\alpha_s \omega}{r^2} \right]^{1/2}$$

and r is the burning rate of the propellant.

The criterion for linear instability of a rocket motor is obtained by setting the denominator of the Green's function g_ω to zero. For small $\bar{M}_e$, terms of the order of $\bar{M}_e^2$ and higher may be neglected. Then, using Eqs. (10) and (17), the criterion for instability becomes

$$k_{00}\sin k_{00}\ell - (ik(\gamma - 1)\bar{M}_e/2)\cos k_{00}\ell = 0 \quad (19)$$

The effect of β is felt through the modified wave number k_{00} according to Eq. (9).

For a given rocket geometry and exit Mach number, the value of β (denoted by β_{crit}) may be obtained that makes the rocket unstable. It is then possible to specify the parameters A and B that yield β_{crit}, given the thermal diffusivity of the propellant and the burning rate law. An example of the stability curve in terms of the parameters A and B is shown in Fig. 9. The calculation assumes the following values:

$$\ell/a = 30, \quad n = 0.65, \quad r = 1 \text{ cm/s}, \quad \gamma = 1.2,$$

$$\bar{M}_e = 0.2, \quad \alpha_s/ca = 7.2 \times 10^{-7}, \quad and \quad \bar{\rho}_s/\bar{\rho}_g = 150$$

As the parameters A and B are varied in a suitable manner (e.g., in the direction of the arrow in Fig. 9), β approaches β_{crit} and the acoustic pressure level in the chamber increases.
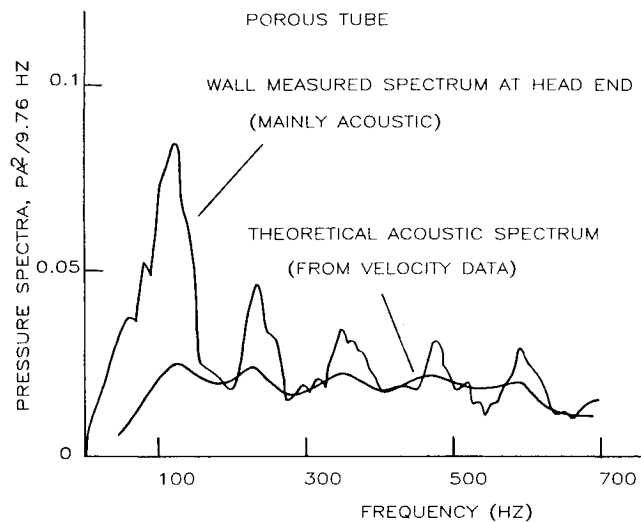
Typical variations in the pressure level may be estimated by scaling the turbulence quantities obtained experimentally.

The scaling is done by assuming that $A^2 S_{00}(x)$ varies as $\rho_0^2 \bar{U}_{1c}^4$ and evaluating the density ρ_0 in terms of the mean pressure and temperature in the rocket chamber via the perfect gas equation. Further, it is assumed that l_{corA}/a remains constant.

A sample calculation is shown in Fig. 10. The mean pressure and temperature inside the rocket motor were taken as 13.8×10^6 Pa and 2500 K. The radius of the motor was taken as 0.05 m. Turbulence levels were scaled from the shortened porous tube configuration. The rocket motor was assumed to have $\bar{M}_e = 0.2$ and $\ell/a = 30$. It is seen that the pressure level becomes significant only very near to a stability limit. Away from the stability limit, the rise in pressure level is not steep but gradual as β tends closer to β_{crit}. But very near to the stability limit, there is a steep increase in the pressure level.

Another interesting result is obtained by considering the nature of the Green's function g_ω. The transformed acoustic pressure [Eq. (11)] may be approximated by applying the same assumptions leading to Eq. (14), resulting in

$$p_{\Phi\omega} \approx -\frac{2\rho_0 l_{\text{corA}}}{A} \sum_{n=0}^{N} k^2 g_\omega(x,x_n) R(\omega,x_n)$$
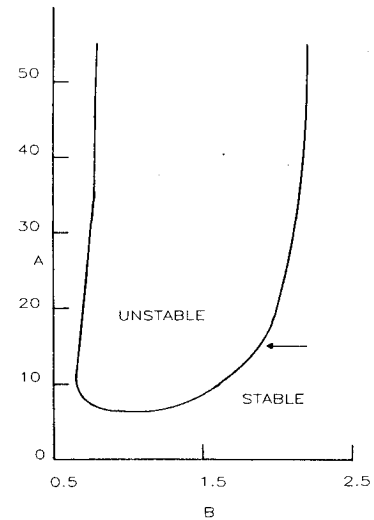

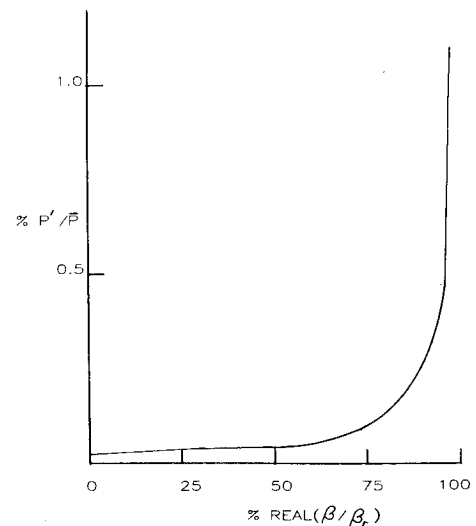Fig. 9 Typical stability limit in terms of the parameters A and B.

Fig. 8 Pressure spectra at head end for basic porous tube.

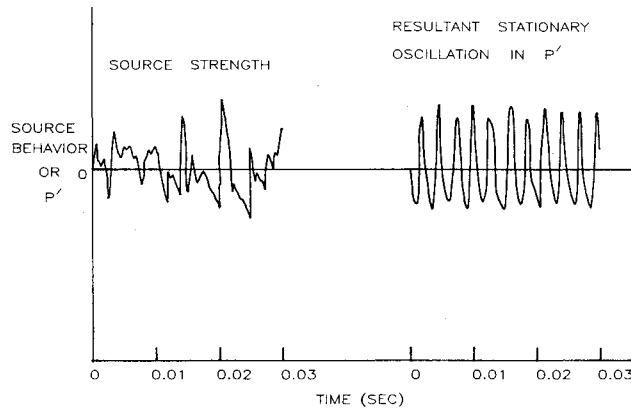Fig. 10 Typical pressure levels as a function of $(\beta/\beta_{\text{crit}})$.

Fig. 11   Action of the Green's function g_ω as a filter.

where

$$x_n = nl_{\text{corA}}, \quad x_N \approx \ell, \quad \text{and}$$

$$R(\omega, x_n) = \int_{A_{(x_n)}} (\bar{U}_l - \bar{U}_{lc}) u_{l\omega} \, dA \tag{20}$$

The inverse Fourier transform of Eq. (20) is

$$p_\Phi(x,t) \approx -\frac{2\rho_0 l_{\text{corA}}}{A} \sum_{n=0}^{N} g_T * R_T \tag{21}$$

where $*$ denotes the convolution operation.

As a simple exercise one term of Eq. (21) corresponding to $x=0$ and $x_N = \ell$ was chosen. The function $g_\omega(0,\ell)$ for a 0.5% pressure level (Fig. 10) was calculated as a function of frequency. The signal from a white noise generator simulated R_T. The inverse Fourier transform of $k^2 g_\omega(0,\ell)$ was convolved with a sample R_T over a time of 0.2 s. The result is shown in Fig. 11. The signal R_T is the source strength for the pressure fluctuations and is a random signal. But when it is operated upon by g_T a periodic signal of nearly constant amplitude results. This occurs because g_T acts like a bandpass filter such that signals at or near the resonant frequencies of the motor are passed unhindered, whereas fluctuations at other frequencies are suppressed. In this numerical experiment, the amplitude of the resulting signal will depend upon the content of the white noise sample chosen. For an actual rocket motor, the pressure fluctuation according to Eq. (21) is given by a sum of convolutions, which will depend on the frequency content of the turbulence over the entire volume of the rocket chamber. For statistically stationary turbulence, the net frequency content of the turbulence over the entire chamber should not vary appreciably with time. Hence, in this case the pressure fluctuations will also be nearly periodic and of nearly constant amplitude.

Conclusion

The generation of sound by turbulence in simulated rocket motor interior flows has been investigated analytically and experimentally. The entire volume of turbulence within the motor cavity is responsible for the generation of acoustic pressure fluctuations. However, it is possible to estimate the pressure spectra from limited data on the turbulence field and from knowledge of the acoustic impedance at flow boundaries. Higher turbulence levels increase the pressure level. If the energy in the turbulence spectrum is high in frequency bands containing resonant frequencies of the motor, the problem may become severe. The increase in the pressure level with the increase in the propellant driving characteristics is very gradual away from a stability limit. Significant pressure levels are generated only extremely close to a stability limit where for all practical purposes the motor may be deemed unstable. However, an interesting result is that, while the driving turbulence is band limited noise, the resulting pressure oscillation is nearly periodic in character.

Acknowledgments

References

[1] Derr, R. L., Mathes, H. B., and Crump, J. E., "Application of Combustion Instability Research to Solid Propellant Rocket Motor Problems," *Solid Motor Technology*, AGARD CP 259, April 1979, pp. 23-1, 23-12.

[2] Yates, J. E. and Sandri, G., "Bernoulli Enthalpy: A Fundamental Concept in the Theory of Sound," *Aeroacoustics: Jet Noise, Combustion and Core Engine Noise*, edited by I. R. Schwarz, MIT Press, Cambridge, Mass., 1976, p. 65.

[3] Strahle, W. C. and Neale, D. H., "Turbulence Generated Pressure Fluctuations in a Rocket-Like Cavity," *AIAA Journal*, Vol. 19, March 1981, pp. 360-365.

[4] Yates, J. E., "Application of the Bernoulli Enthalpy Concept to the Study of Vortex Noise and Jet Impingement Noise," NASA CR 2987, April 1978.

[5] Morse, P. M. and Ingard, K. U., *Theoretical Acoustics*, McGraw-Hill Book Co., New York, 1968.

[6] Laufer, J., "The Structure of Turbulence in Fully Developed Pipe Flow," NACA TR 1174, 1954.

[7] Hegde, U. G., "Turbulence Generated Pressure Fluctuations in a Class of Interior Flows," Ph.D. Thesis, Georgia Institute of Technology, Atlanta, Ga., 1983.

[8] Komerath, N. M., Hegde, U. G., and Strahle, W. C., "Turbulent Static Pressure Fluctuations Away from Flow Boundaries," AIAA Paper 83-0754, April 1983.

[9] Culick, F.E.C., "A Review of Calculations for Unsteady Burning of a Solid Propellant," *AIAA Journal*, Vol. 6, Dec. 1968, p. 2241.